



Supplement of

Failure of Marmolada Glacier (Dolomites, Italy) in 2022: data-based back analysis of possible collapse mechanisms

Roberto Giovanni Francese et al.

Correspondence to: Aldino Bondesan (aldino.bondesan@unipd.it)

The copyright of individual parts of the supplement might differ from the article licence.

S1 Introduction

The detailed study of the Marmolada failure was possible through the construction of a large digital database of the glacier including glaciological and meteo-climatic data, historical cartography, modern numerical cartography, aerial and satellite images, geophysical images, geological and geomorphological data collected over the last 20 years (Table S1).

S2 Geology and morphology

The Marmolada massif, located in the Eastern Alps in Italy (Fig. S1), is primarily composed of Ladinian limestone, specifically the Calcare della Marmolada, which is part of the Dolomia dello Sciliar formation (Antonelli et al., 1990; Bosellini, 1996). This massif provides a stratigraphic record of the Dolomites' complex geological history, including remnants of Paleozoic volcanism and Triassic carbonate platform development. The massif exhibits a monoclinical structure, characterized by northward-dipping bedding planes, which contribute to its stepped morphology known as "cuesta."

The Marmolada massif is bounded by several major valleys, including the Ombretta, Contrin, Avisio, and Pettorina valleys. The southern flank is marked by a near-vertical fault that extends through the Ombretta Valley, forming one of the highest and most challenging climbing walls in the Alps, nearly 1000 m high. Evidence of past glacial activity is widespread (Carton and Varotto, 2011), with geomorphological features such as moraine ridges, roches moutonnées, hanging valleys, and glacial cirques preserved across the landscape (Carton et al., 2017; Bondesan & Francese, 2023). The massif also preserves evidence of ancient geological processes, from Permian volcanic activity to Triassic tropical atoll environments, highlighting its significance in understanding the broader geodynamic evolution of the Dolomites (Bosellini, 1996).

During World War I, the Marmolada Glacier played a strategic role as Austro-Hungarian forces excavated an extensive network of tunnels and underground defenses within the ice, accommodating approximately 300 soldiers (Bondesan et al., 2015). Today, remnants of these wartime structures are occasionally uncovered due to ongoing glacial melting.

S3 Data and methods

S3.1 Climatic variables

Time series of temperature, rainfall and snow cover were provided by ARPAV. Stations (Fig. S2 and Table S2) from two different networks were considered. Malga Ciapela (MAO), Punta Rocca (PRC), Passo Pordoi (PPR) and Arabba (ARB) belong to the standard meteorological network (sampled parameters: temperature, precipitation, wind, and humidity) while M.A. Ornella (MAO), C. Pradazzo (CPR), C. Baldi (CBL), Ra Valles (RVL) and Piz Boé (PZB) are part of a specific "snow & avalanche forecasting" network (sampled parameters: temperature, precipitation, wind, humidity, solar radiation, thermal gradient in the snowpack, albedo and snow thickness). A 30m deep borehole was drilled in 2010 nearby the PZB station and it was equipped with a T probe. Base analysis was conducted over the period 1990-2020 (a 31-year reference), to spot anomalies and compare the average yearly and monthly trends with the 2022 records. About 7.9% of the values were missing in the temperature time series while in the rainfall and snow cover time series were missing 0.8% and 2.1% of the values respectively (see Table S2 for time series completeness).

Missing data were either retrieved from other sources (ENEL, PAT, REVEN, etc.) or estimated from nearby stations using various prediction techniques (Acock & Pachepsky, 2000; Kotsiantis et al., 2006). In addition to guess the temperature of long missing intervals monthly correlation functions were calculated between station pairs. Four pairs (MAO-MCP; MCP-PRC;) required the calculation of 144 functions (4 pairs * 12 months * 3 T values – min, avg, max). Once the correlation algorithm was implemented (MATLAB, 2018) the misfit between observed and predicted values was graphed (Fig. S3). Each missing monthly interval was then restored using the algorithm with the minimum misfit.

Late spring and early summer of 2022 proved to be a particularly anomalous period (Fig. S4), with three months (May, June, and July) during which average temperatures exceeded the standard deviation range. The most significant deviation occurred in June, when the maximum temperature was approximately 4.5 degrees higher than the reference line (1990–2020). Also in the spring–summer of 2003, particularly anomalous conditions were observed (Fig. S4), with complete glacier snow cover loss and abundant meltwater production. However, the period of positive deviation from the standard deviation range lasted only one month (June), with a deviation of 3.5 degrees with respect to the reference line (1990–2020).

S3.2 Permafrost

The modeled permafrost occurrence (on a 25 m by 25m grid) in the Marmolada massif (Boeckli et al., 2012) indicates permafrost conditions at and around the failure site. With such estimated surface temperatures, permafrost depth could be significantly deep. Borehole temperatures compiled for comparable surface temperatures could exceed 100 m of depth (Etzel Müller et al., 2020).

S3.3 Glaciological data

These data mostly refer to the periodic measurements of the xyz position of the glacial front at specific sites. The Italian Glaciological Committee, (born as a working group of the Italian Alpine Club – CAI in 1895) is responsible for such measurements and annual bulletins of the glaciological campaign were yearly published since 1914.

First measurements in the Marmolada glacier date back to 1971 and these measures were systematically organized since 1985. Dxyz (inclined distance) and Dz (vertical distance) were taken from specific benchmarks during each campaign. The glacier was divided in three sectors (eastern, central and western) and a single benchmark was located in each sector (Fig. S5). The records are almost complete and just few years are missing.

S3.4 DTMs-Digital Terrain Models

Several types of DTMS were generated for the purpose of estimating the time-lapse reduction of the ice area/surface/volume (Fig. S6) by aid of: historical cartography, aerial/satellite images, numerical cartography and LIDAR (Light Detection and Ranging) data (see Table S5 for available data sources).

DTMs of the glacier surface

DTMs for the years 1905 1954, 1971 were obtained digitizing the elevation contours after proper geo-referencing of the map. Geo-referencing result was affected by errors mostly caused by cartographic distortion despite the elevate number of control points. A maximum of 10 m shift was observed (Table S3). As an example the overall geo-referencing RMSE for the 1905 map was equal to 10.6 m (Bondesan & Francese, 2023 – Supplementary Information).

DTMs for the years 1982, 1994, 2000, 2006 were obtained by image correlation (Siebert et al., 2014). This process runs under the same basic conditions as stereoscopic photogrammetry. A series of overlapping images are used in order to get a 3D model of the study area. This model is then tuned and validated using a series of ground control points (GCP). As an example the final RMSE for the 1982 map was equal to 4.8 m (Bondesan & Francese, 2023 – Supplementary Information).

The DTM for the year 2015 was directly obtained by LIDAR data while the DTMs post-2015 were again constructed via image correlation techniques.

DTM of the outcropping bedrock

The DTM of the outcropping bedrock was realized merging digital contour lines from CTP and from CTRNV and including several other key points (topographic peaks and troughs) as well as undersampled LIDAR datasets.

Gridding was obtained via a standard Kriging algorithm with a variable search radius from 2 m to 20 m according to data density. Using this approach, the weight factors were calculated in such a way that the estimation error in each output node was minimized (Krige, 1996). DTMs were finally interpolated over an identical grid geometry (cell size: 2.5 m) prior to undertake area, surface and volume calculations.

The high-resolution DTM of the failure zone and of its surroundings was constructed via a process of data fusion. Satellite stereo imagery (Table S5) and UAV (Unmanned Aerial Vehicle) LIDAR data were used to reconstruct the residual surface of the glacieret, the detachment niche and the rocks surroundings the niche. Several LIDAR datasets (PAT 2009, ARPAV 2014 and PAT 2014) as well as digital cartography (CTRVN 2001, CTP 2015, CTP 2020), associated with several topographic points, were used to reconstruct the morphology of the outcropping rocks of the slope immediately below the detachment. The same datasets were utilized to reconstruct the morphology of the rocky ridge above the failure. LIDAR data also served as a vertical reference datum for correcting the satellite imagery DTM. The process resulted in a grid of 355 m by 490 m with 0.5 m of aperture.

S3.5 Subglacial bedrock (glacier bed) model

Ice-covered bedrock was modeled via high-resolution geophysical imaging. GPR (Ground Probing Radar) mapping along with Multisource ERT (Electrical Resistivity Tomography) were the best survey choices (Fig. S7).

GPR data were collected during five different campaigns (Table S4) by use of:

- a single channel radar device, namely GSSI Subsurface Interface Radar 4000, equipped with antennas operating at 70 MHz (unshielded) and 200/500 MHz (shielded). The nominal wavelength (λ) in alpine ice is equal to 2.1 m, 0.8 m and 0.3 m respectively. Vertical resolution could be estimated in $\lambda/4$ - $\lambda/8$ (Widess, 1973);
- a multi-channel radar system, namely IDS Stream X operating simultaneously 15 channels and equipped with bistatic antennas operating at 200 MHz;
- a single-channel radar system, namely PULSEKKO IV, equipped with a bistatic antenna operating at 100 MHz (Pasta et al., 2004);
- a single-channel radar system, namely GSSI Subsurface Interface Radar 3000, equipped with an unshielded monostatic antenna operating at 35 MHz (Pasta et al., 2004).

The signature of the ice-bedrock interface was more or less sharp all over the glacier but nearby the Marmolada crest where electro-magnetic signal scattering was observed during various surveys. The radar device was always coupled with a geodetic GPS (Global Positioning System) device to accurately survey GPR scan position.

ERT data were collected with a MultiSource system (LaBrecque et al., 2013; Bocchia et al., 2021). It comprises several stand-alone transceivers synchronized via GPS timing and controlled via a 900 MHz radio signal. The primary feature of this system is its capability of transmitting the current simultaneously with multiple dipoles thus resulting in a better illumination of the buried targets.

S3.6 DTM error estimation

Several sources of errors should be considered in the generation of the DTMs: cartography; geo-referencing distortion, geophysical and topographical instrument accuracy, positioning, etc. A rough estimate of the major errors is summarized in Table S3 and Table S4.

Area - A

A quick calculation could be done considering the glacial area A equivalent to the area of a rectangle with sides $x \pm \Delta x$ and $y \pm \Delta y$ where Δx and Δy are the uncertainties of the surface point position in the two directions. The relative error $\Delta A/A$ could be expressed as:

$$\frac{\Delta A}{A} = \frac{\Delta x}{x} + \frac{\Delta y}{y}; (S1)$$

and

$$\Delta A = A \left(\frac{\Delta x}{x} + \frac{\Delta y}{y} \right) = xy \left(\frac{\Delta x}{x} + \frac{\Delta y}{y} \right) = y\Delta x + x\Delta y; (S2)$$

In case of a glacial area A equivalent to the area of a square the two errors could be considered equal ($\Delta x = \Delta y$). In this case the relative error $\Delta A/A$ is:

$$\Delta A = A \left(2 \frac{\Delta x}{x} \right) = x^2 \left(2 \frac{\Delta x}{x} \right) \rightarrow \Delta A \approx 2\Delta x\sqrt{A}; (S3)$$

Volume - V

A quick calculation could be done considering the glacial volume V equivalent to the volume of a prism of rectangular area A and average thickness $\bar{z} \pm \Delta z$, where Δz is the uncertainty in the vertical direction. The volume V could be expressed as $A\bar{z}$ and considering equation (S2):

$$\Delta V = \bar{z}\Delta A + A\Delta z = \left(\frac{V}{A} \right) \Delta A + \Delta z; (S4)$$

In case the rectangle A is a square equation (S4) could be simplified as follows:

$$\Delta V \approx \frac{2V}{\sqrt{A}} \Delta x + A\Delta z; (S5)$$

The overall errors related to area/surface/volume calculations were then estimated with the above equations.

S3.7 Glacial front and area, surface and volume calculations

Area, surface area and volume quantities were computed for the following years: 1880, 1905, 1954, 1971, 1982, 1994, 2000, 2006, 2015, 2017, 2019 and 2021. For the reconstruction of the glacier in the year 1880, three different cartographic sources were used, as none of them contained complete data.

The glacier perimeter (Fig. S6) was directly extracted from the DTMs or from the geo-referenced aerial and satellite images (Table S5). Direct measurements of the glacial front (collected during the annual CGI campaign) were used to constraint and validate the process. The digital models of the time-varying glacial surface and of the buried bedrock allowed for the computation of area, surface and volume changes undergone over time.

The first quantity to be computed was the area of the glacier. The quantity was directly computed by projecting the xyz boundary on a horizontal plane. In case of multiple glacier units, the overall area was obtained summing partial areas while in case of rock windows the area of each rock window was subtracted from the sum. The computed areas are comparable with the values provided by other authors (Varotto and Ferrarese, 2011).

The surface of the glacier was computed on the 3D models as the cumulative area of the triangles forming the TIN (Triangular irregular Network) approximation of the glacial surface.

The ice volume was finally computed using the top/bottom (bedrock/glacier) surfaces enclosed by the glacier perimeter.

S3.8 Ice and snow melting prior to collapse

The mean melt rates in the weeks precedent to the collapse were computed via the degree-day model (Pellicciotti et al., 2005; Wang et al., 2019) using the solar global daily radiation provided in the Italian Atlas of the solar radiation (ENEA, 2023) and corrected for the presence of surface

debris (Xue et al., 2020). Details on the calculations are provided in the Supplementary Information of Bondesan & Francese, 2023. Based on these calculations, crevasses could quite safely be considered water-filled at the time collapse occurred.

S3.9 Satellite imagery

Pre- and post-event (Fig. S1) satellite images were taken by the Pléiades Neo constellation (AIRBUS Defence & Space), pansharpened, pancromatic 30 cm native GSD; 6 multi-spectral channels, 1.2 m native GSD. Pancromatic sensors span from ~450 nm to ~800 nm; multispectral sensors span from ~380 nm to ~880 nm.

A pre-failure shot was taken on Jun 20, 2022, h 10:06:67 GMT while two post-failure shots were taken on Jul 8, 2022, h 10:02:07 GMT and Jul 9, 2022, h 10:20:21 GMT respectively.

Details about coarse and fine orthorectification and geo-referencing along with processing errors are provided in the Supplementary Information of Bondesan & Francese, 2023.

Additional processing was required to get a better insight on specific features. The resolution of each normalized band was increased by a factor 3 to provide the user with a better readable picture on a 4k display. This is a critical step in which only minimal alterations of the image spectral contents are acceptable. Different techniques can be exploited to balance the user's perceptual experience with the fidelity to the data; they range from bicubic interpolation to methods based on machine learning such as convolutional neural networks (CNN) (Liebel et al., 2016) or generative adversarial networks (GAN) (Ledig et al., 2017). In this study a Lanczos-3 interpolation kernel was used, since it provides a good compromise between visual image quality and the introduction of undesired spectral components; it has also already proved to be effective on remote sensing images (Madhukar et al., 2013).

The high frequency content of each normalized band was then enhanced by subtracting from the data the output of a linear Gaussian filter having standard deviation equal to 0.9 and a gain factor of 2.

The Normalized Difference Water Index (NDWI) was finally calculated. For this index two definitions can be used, based respectively on the difference between the NIR and blue bands (Huggel et al., 2022), or the NIR and green bands (McFeeters, S.K., 1996). In our experiments the latter was chosen, since it can detect also melt water on glaciers and water-rich soil (Aggarwal, 2016).

S3.10 Seismology

The failure-generated earthquake was located using an automatic routine based on the HYPO71 algorithm (Lee & Lahr, 1975) that mostly uses logic and arithmetic resulting in high computational efficiency. Additional information was retrieved via the filter picker algorithm (Lomax et al., 2012). The time-frequency analysis of the event (Fig. S8) exhibits signals in the 1.5–5 Hz interval, with longer-lasting shaking visible in the H2 channel (AGOR E). Because the failure occurred close to the surface, the seismic records are dominated by the horizontal component of Rayleigh and Love waves. The first major impact on the glacier surface appears at about 25 s (showing a frequency peak around 3 Hz mostly visible in the H2-channel). Most of the energy is released in the range between 50 s and 80 s (with a spectral band of 3-4 Hz but including also frequencies lower than 2 Hz) and it is visible in the horizontal channels H1 and H2 (AGOR N, E). The higher frequencies are probably to be correlated with the spreading of the ice debris on the lower glacial surface at 2500-2600 m asl. A diffuse band (in the frequency range lower than 2 Hz) of weak amplitudes is outlined in the vertical channel Z (AGOR V). These signals are present in the entire wave train but, due to the lack of constraints, they should be better classified as background noise.

S3.11 Airborne thermal infrared (IR) imaging

Some IR images of east-west segment of the failure surface were taken on Oct 14, 2022 at approximately 7:00 AM CET. The IR images were recorded using a NEC avionic thermo tracer H2640 (Fig. S9). The infrared detector is an uncooled focal plane array (microbolometer) with a spectral range from 8µm to 14 µm and an accuracy of ±2%.

The camera was mounted on the side of a helicopter with the sensor kept more or less parallel to the failure surface and the shots were taken at a distance of approximately 20-25 m from the failure face. The images were processed using the NRG. The minimum air temperature recorded during the night before the measurements was -3.5°.

S3.12 Back analysis and overall slope stability

Glacier stability was assessed by means of the Limit Equilibrium Method (LEM), which is routinely used for slope stability analyses in geotechnical engineering. LEM considers the equilibrium of a rigid body, such as the slope or the glacier in this case, along a slip surface of any shape. From this equilibrium, the driving actions are calculated and compared to the available resistance calculated according to Mohr-Coulomb's shear strength criterion. From this comparison, the Factor of Safety (FoS) is derived. FoS is the ratio between resisting and driving actions:

$$FoS = \frac{\text{resisting actions}}{\text{driving actions}}; (6)$$

The lower the FoS the higher the possibility of instability and collapse. In particular, if FoS is less than one, the slope is unstable and FoS = 1 is assumed as the limit stability value. Among the variety of methods of slices available to determine FoS, three different methods were used in this analysis, namely, Janbu simplified (J) (Janbu et al., 1956), Janbu corrected (Jc) (Janbu, 1954; 1973), and GLE/Morgenstern-Price (Morgenstern and Price, 1965). The stability analyses have been computed using the Slide2 software (Rocscience®) considering different scenarios to assess, by back analysis, the conditions that plausibly led to the collapse of the glacier.

Software packages

Seismic Un*x package R4426

GoCad 7.0

Matlab R2022a

Autocad Map 3D 2022

ArcMap 10.8.1

Surfer 22.0

Origin 8.1.9

Catalyst 2222.0.6

Slide2 9.027

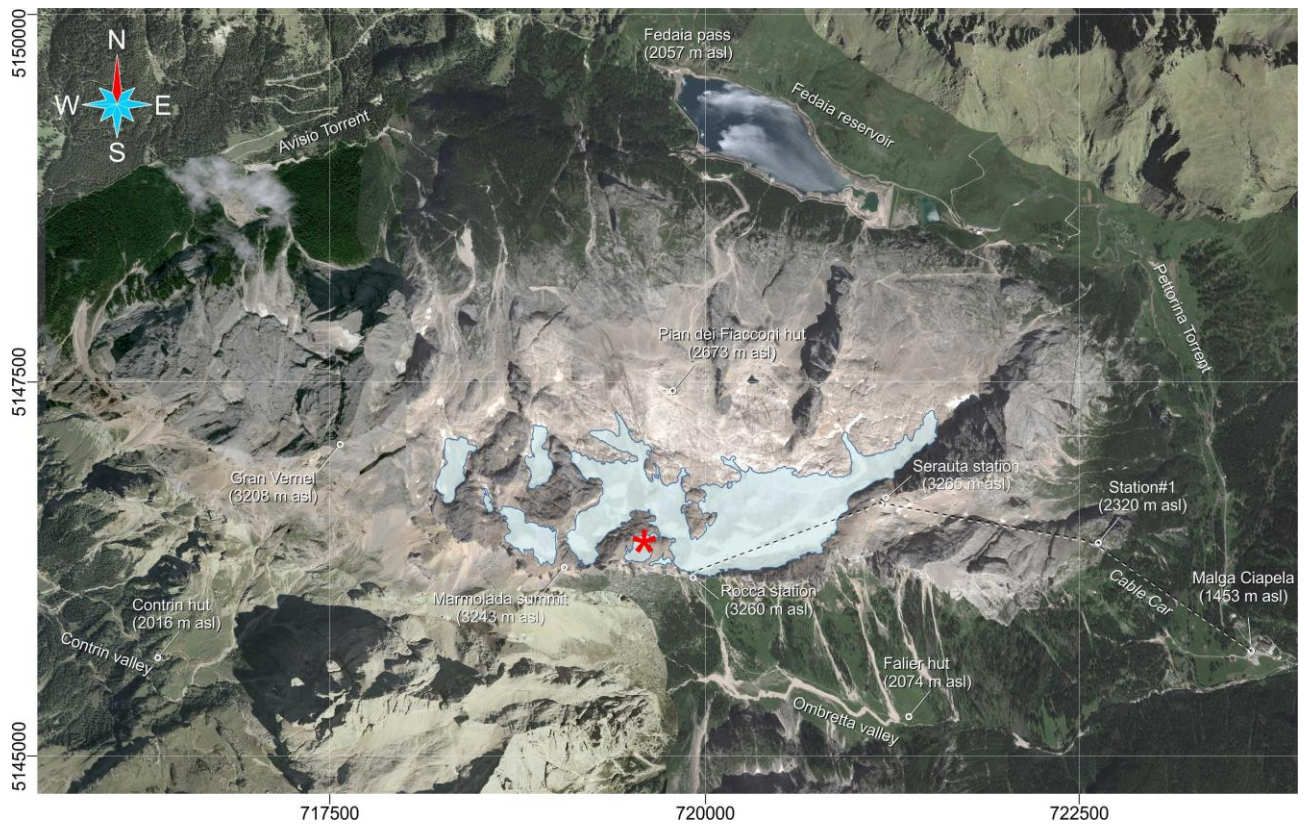


Fig. S1. Satellite ortomosaic of the Marmolada Massif. Date of acquisition: July 8 and July 9, 2022, Pléiades Neo, AIRBUS Defence & Space. The red asterisk marks the failure. Aerial and satellite imagery source: Pléiades Neo, AIRBUS Defence & Space; Autonomous Province of Trento (PAT).

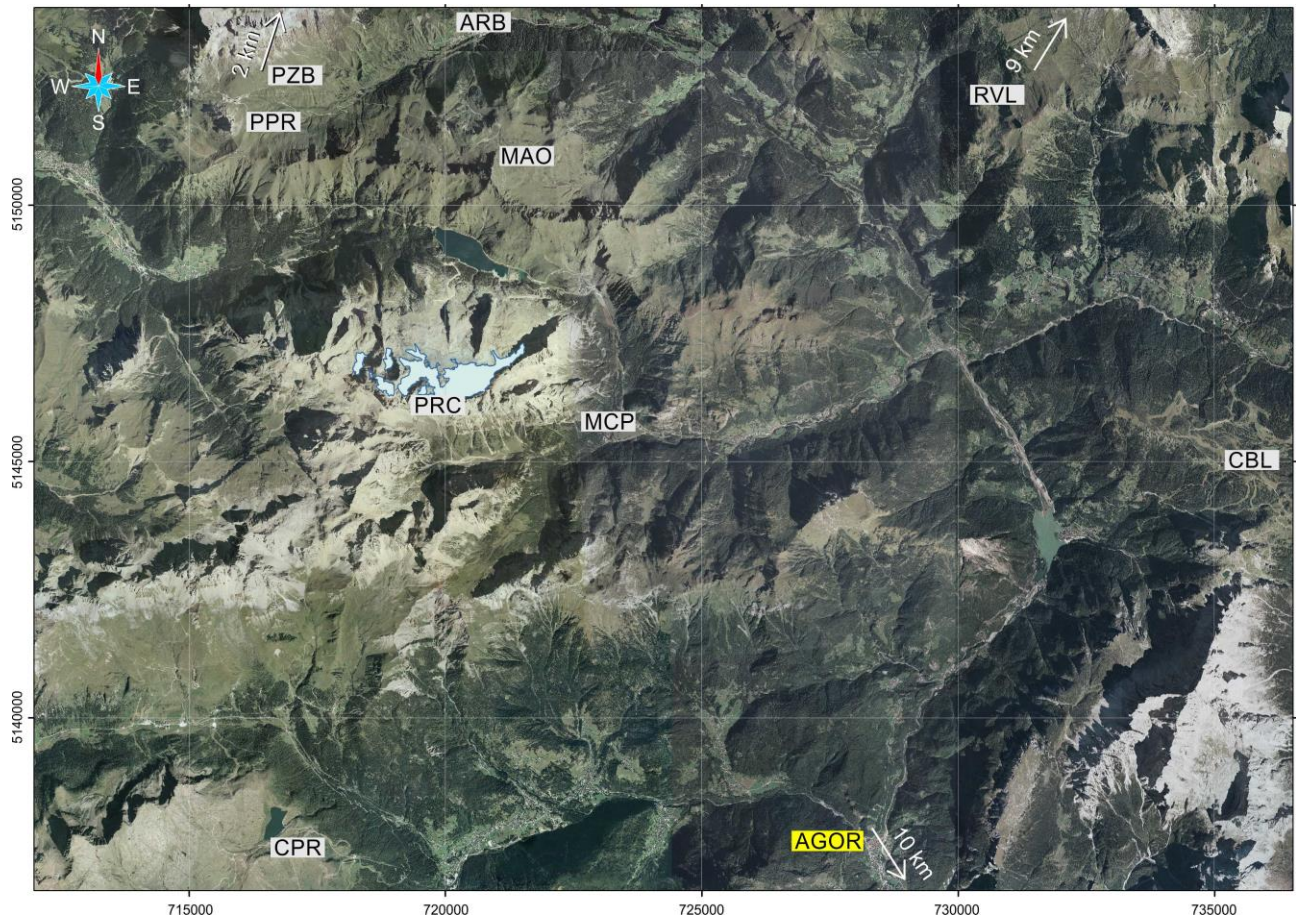


Fig. S2. Aerial image with indicated the meteorological stations located around the Marmolada massif. ARB – Arabba (R); PPR – Pordoi pass (R); MCP – Malga Ciapela (R,T); PRC – Punta Rocca (T); CPR – Cima Pradazzo (T,S) and CBL – Col dei Baldi (T,S); PZB – Piz Boé (S); RVL – Ra Valles (S). T=Temperature, R=Rainfall, S=SnowThickness; AGOR: Seismological station (see also Table S2). Aerial and satellite imagery source: Autonomous Province of Trento (PAT).

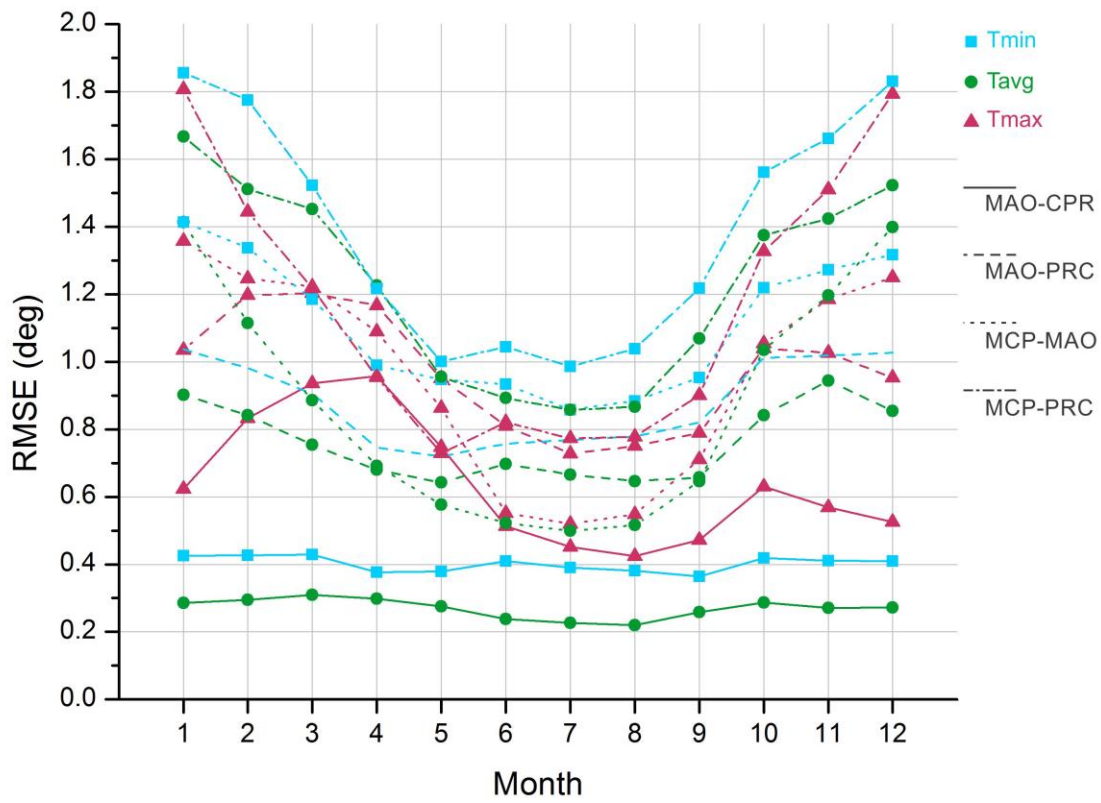


Fig. S3. RMSE of the correlation function between station pairs. Missing data points of the temperature time series were computed using the correlation function with the minimum misfit for that specific month.

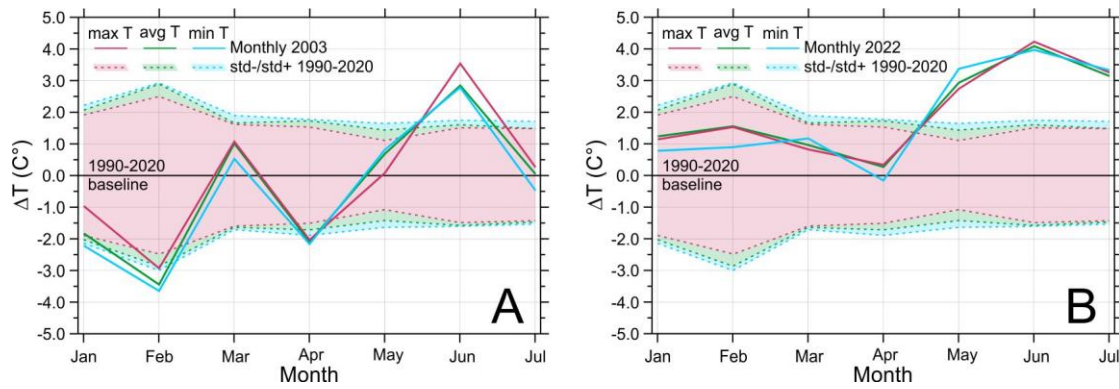


Fig. S4. Comparison between the monthly averages of the year 2003 (A) and those of 2022 (B), relative to the mean values of the ~30-year reference period 1990–2020. In the year 2022, a three-month period was observed with values above the standard deviation range, with a maximum positive deviation in the maximum temperature of approximately 4.3 $^{\circ}\text{C}$ compared to the reference line. In contrast, in the year 2003, only one month was observed to be above the standard deviation range, with a positive deviation of approximately 3.5 $^{\circ}\text{C}$.

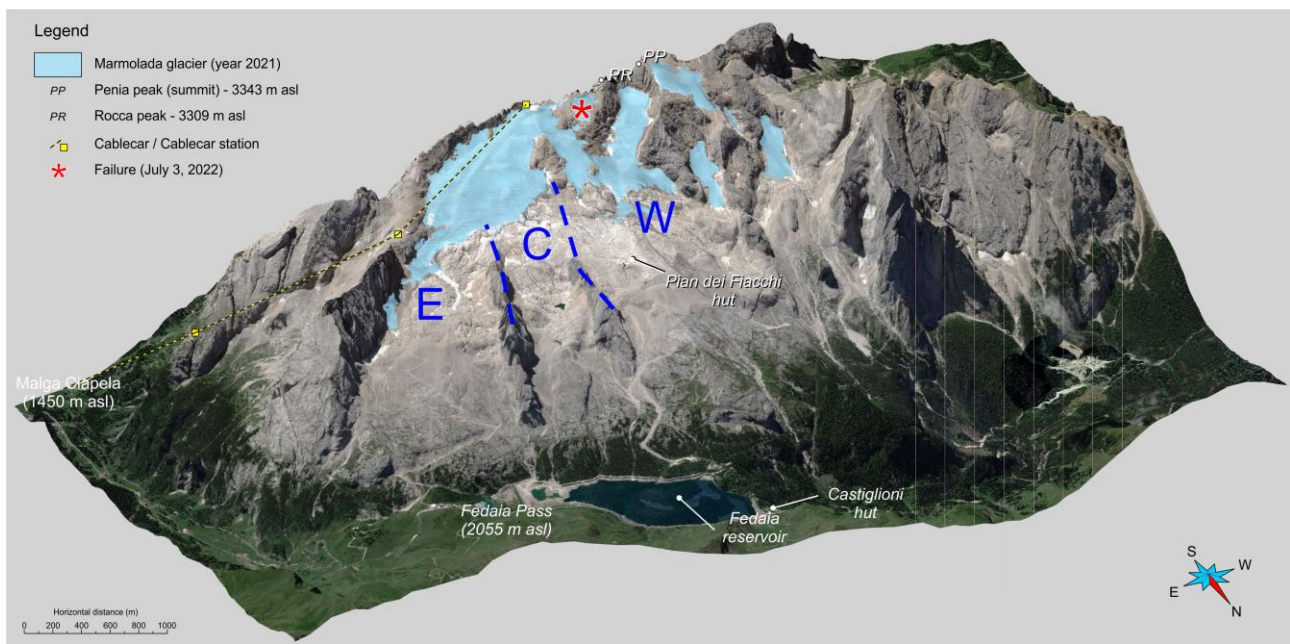


Fig. S5. Glaciological partition of the Marmolada glacier. E – eastern sector; C – central sector; W – western sector. Reference points are available for each one of the three sectors. Aerial and satellite imagery source: Pléiades Neo, AIRBUS Defence & Space; Autonomous Province of Trento (PAT).

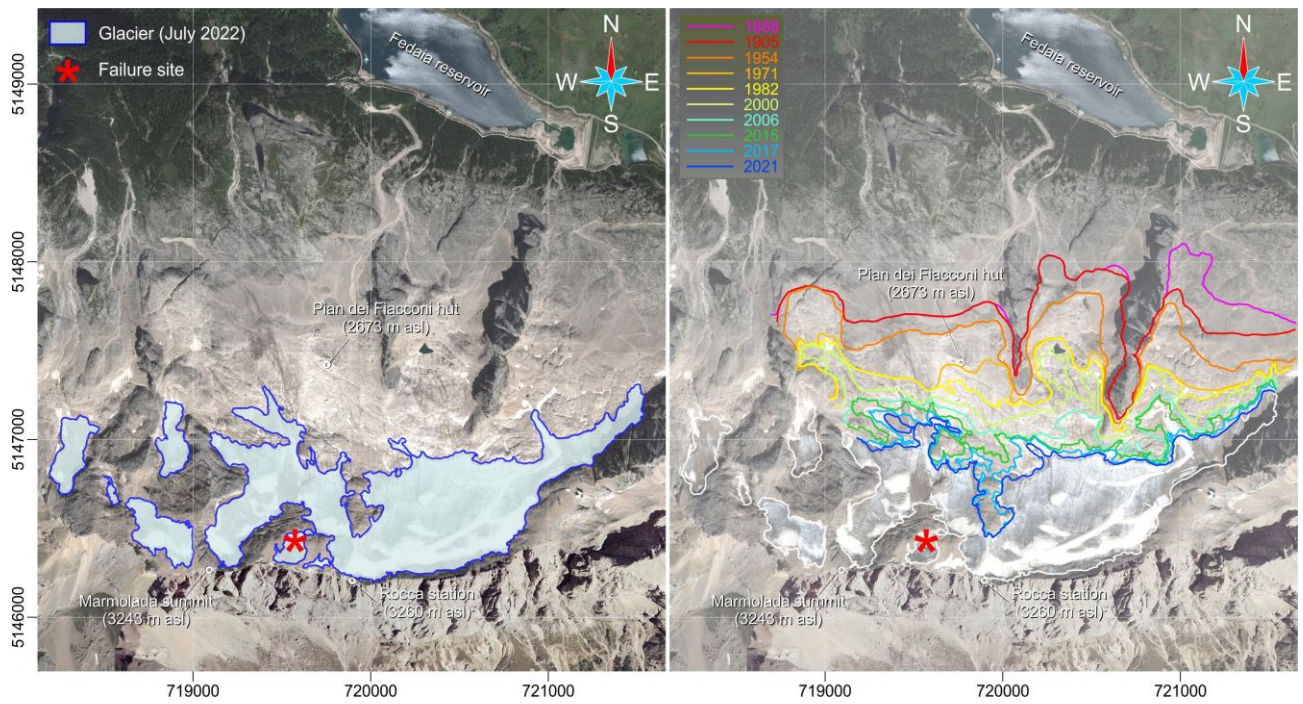


Fig. S6. Marmolada glacier (left panel) and front migration over the period 1880-2021 (right panel). Basemap: Pléiades Neo, AIRBUS Defence & Space (date of acquisition: July 8 and July 9, 2022). The detachment zone is marked with an asterisk. The 2022 glacier evidenced in both panels (blue outline and light blue fill on the left; white outline on the right). Aerial and satellite imagery source: Pléiades Neo, AIRBUS Defence & Space.

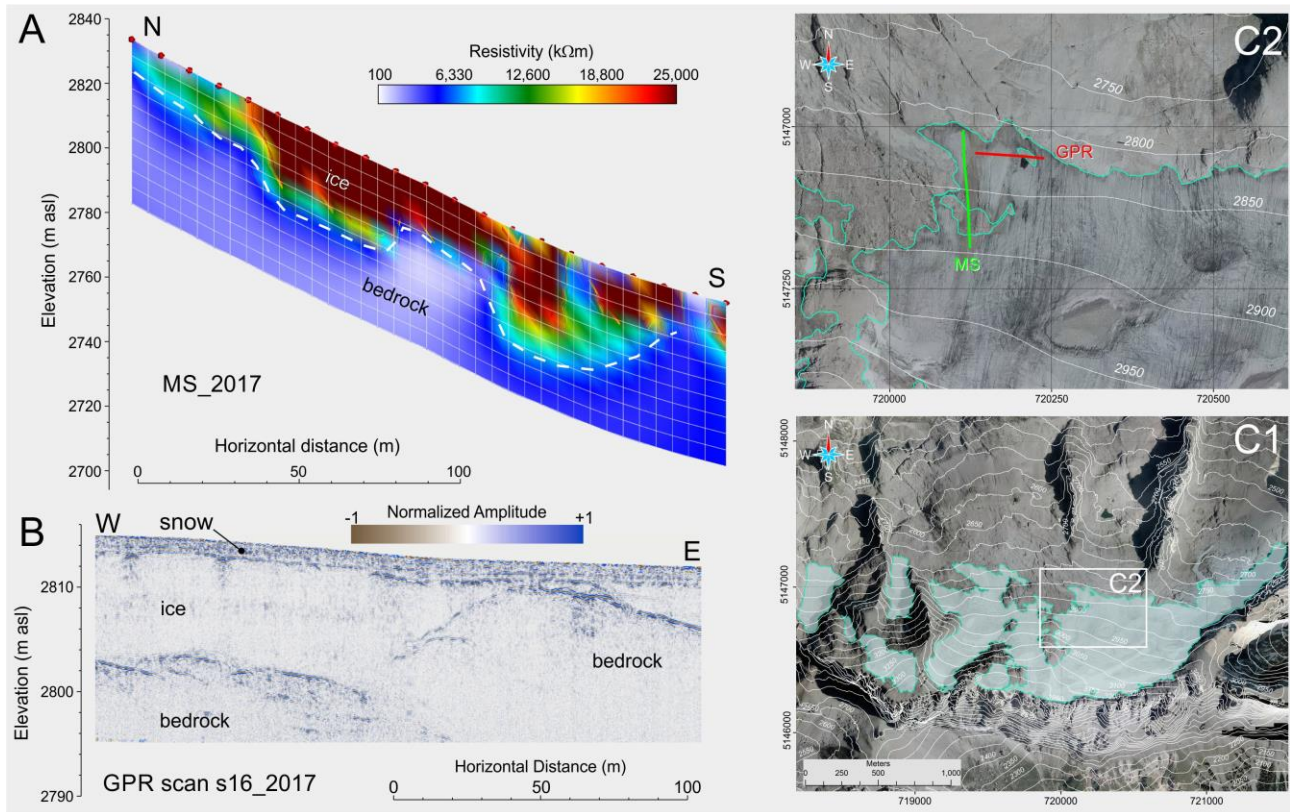


Fig. S7. Geophysical surveys on the Marmolada Glacier. Ice-covered bedrock was modeled via high-resolution geophysical imaging. Data were collected in five different campaigns from 2004 to 2022. Multisource ERT (A) and GPR (B) were utilized to outline geometry and properties of buried bedrock and ice. (C) Map showing geophysical profiles (panel A and panel B) collected during the 2017 campaign.

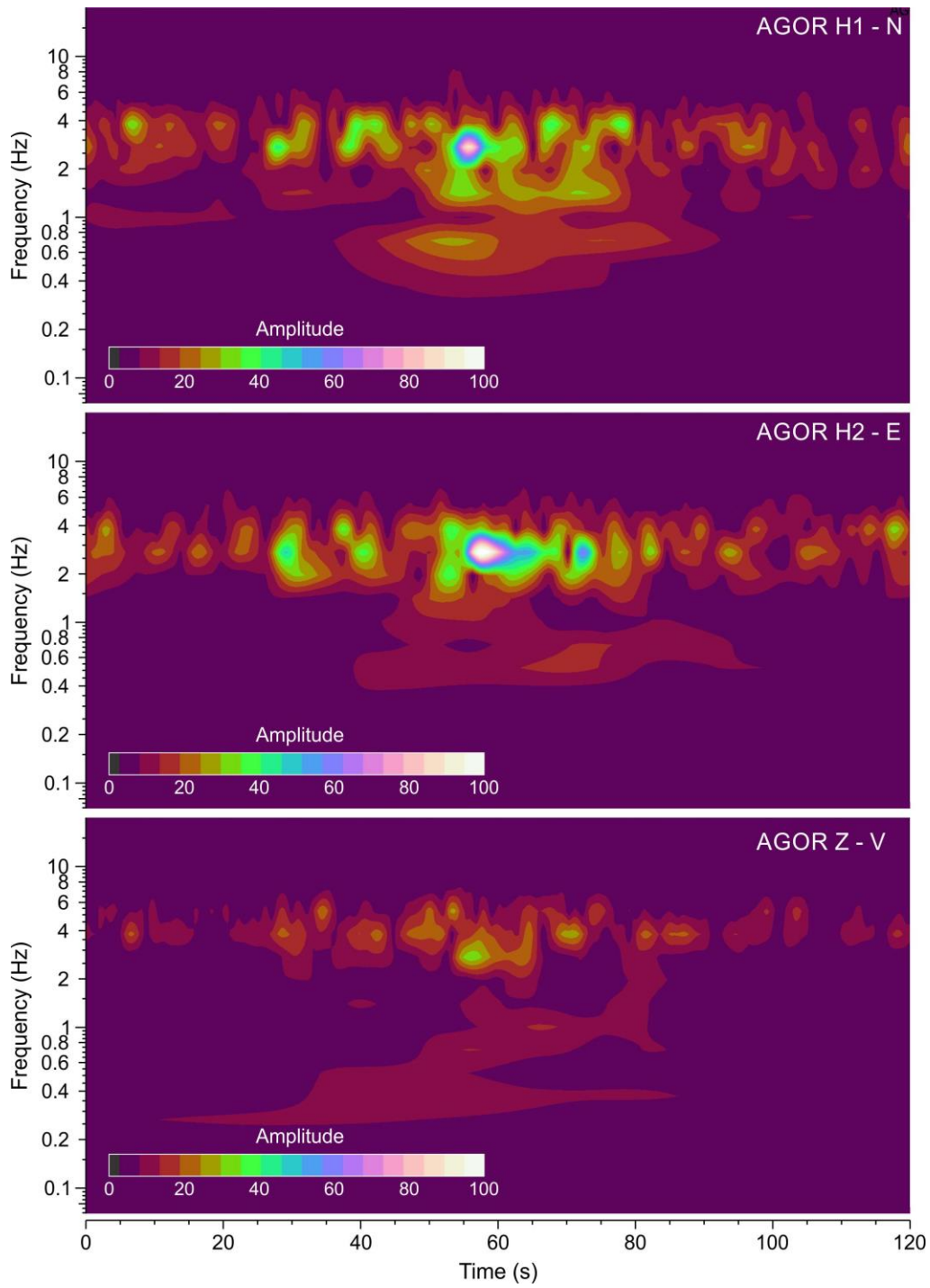


Fig. S8. Time frequency analysis of the failure-generated earthquake. (Top panel) – horizontal N component; (Middle panel) horizontal – E component; (Bottom panel) vertical – Z component.

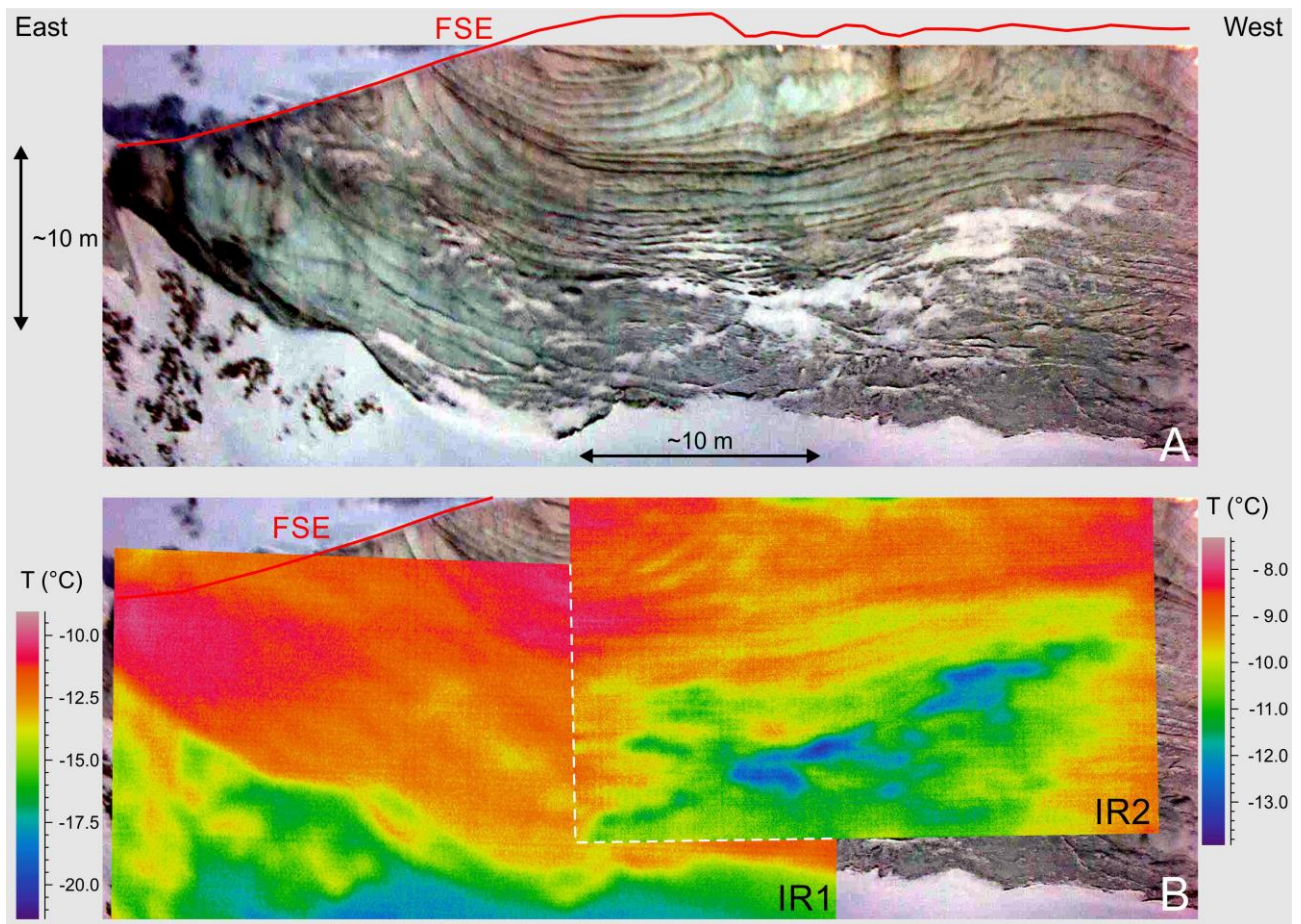


Fig. S9. Uncalibrated IR image of the north face of the failure scarp taken on Oct 14, 2022. The IR images were taken on Oct 14, 2022 at approximately 7:00 AM CET with a NEC Thermo Tracer H2640. (A) Photomosaic of RGB images; (B) shots IR1 and IR2 overlaid on the RGB image. FSE: Failure Scarp Edge. Snow is clearly biased cold.

Table S1. Digital database of the Marmolada massif. LIDAR - Light Detection and Ranging; TLS - Terrestrial Laser Scan; GPR – Ground Probing Radar; EMI - Electro-Magnetic Induction; ERT – Electrical Resistivity Tomography; MAG – Gradiometry.

| Time span (years) | Data source | Data collector | Type | UM | Value |
|----------------------|------------------------------------|-------------------|---------------------------------|----|-------|
| 1871-1932 | Historical cartography | seeTable S5 | Geo-referenced digital image | n | 8 |
| 1932-1977 | Cartography | seeTable S5 | Geo-referenced digital image | n | 2 |
| 1977-2021 | Modern digital cartography | seeTable S5 | Raster/shapefile | n | 6 |
| 1945-2017 | Aerial images | seeTable S5 | Geo-referenced digital image | n | 19 |
| 2019-2022 | Satellite images | seeTable S5 | Geo-referenced digital image | n | 5 |
| 2009-2022 | LIDAR & TLS | seeTable S5 | Binary | n | 5 |
| 2004-2022 | Geophysics (GPR), | seeTable S5 | Binary | km | 77.9 |
| 2015-2017 | Geophysics (MAG), | seeTable S5 | Binary | km | 1.5 |
| 2015-2017 | Geophysics (EMI & ERT) | seeTable S5 | Binary | km | 1.7 |
| 1985-2022 | Snow and meteorological station | | ASCII time series | n | 9 |

Table S2. Weather stations. T=Temperature (min, max, avg), R=Rainfall, S=SnowThickness, P=Permafrost.

| Station | Elevation (m asl) | Distance from failure (km) | Sampling | Processed parameters | Completeness (%) | Time span (years) |
|---------|----------------------|-------------------------------|----------|-------------------------|---------------------|----------------------|
| PRC | 3250 | ~0.4 | daily | T | 75.4 | 1990-2022 |
| MCP | 1475 | ~3.6 | daily | T | 99.7 | 1990-2022 |
| “ | “ | “ | “ | R | 99.8 | 1990-2022 |
| MAO | 2227 | ~4.9 | daily | T | 96.1 | 1990-2022 |
| “ | “ | “ | “ | S | 98.4 | 1990-2022 |
| PPR | 2154 | ~6.1 | daily | R | 98.4 | 1990-2022 |
| ARB | 1642 | ~6.9 | daily | R | 99.4 | 1990-2022 |
| PZB | 2905 | ~8.6 | daily | S,P | 100 | 2011-2022 |
| CPR | 2195 | ~9.3 | daily | T | 97.1 | 1990-2022 |
| “ | “ | “ | “ | S | 97.5 | 1990-2022 |
| RVL | 2615 | ~21 | daily | S | 100 | 2021-2022 |
| CBL | 1915 | ~16 | daily | T | N/A | 1990-2022 |

Table S3. Data processing strategy for the reconstruction of the glacial surface. HM – geo-referenced historical map; GM – geo-referenced map; ASI – aerial/satellite images; LIDAR – light detection and ranging.

| Year | Data source | Process | Mesh (m) | Expected errors (m) | | | |
|------|-------------|------------------------------------|----------|---------------------|-----|-----------------|-----|
| | | | | Cartography | | Geo-referencing | |
| | | | | xy | z | xy | z |
| 1880 | HM | Digitization of glacier boundary | 10 | 100 | N/A | 25 | N/A |
| 1905 | HM | Digitization of elevation contours | 10 | 25 | N/A | 10 | N/A |
| 1954 | GM | Digitization of elevation contours | 10 | 15 | N/A | 10 | N/A |
| 1971 | GM | Digitization of elevation contours | 10 | 5 | N/A | 5 | N/A |
| 1982 | ASI | Generation of 3D point cloud | 5 | N/A | N/A | < 5 | < 5 |
| 1994 | ASI | Generation of 3D point cloud | 5 | N/A | N/A | < 5 | < 5 |
| 2000 | ASI | Generation of 3D point cloud | 5 | N/A | N/A | < 5 | < 5 |
| 2006 | ASI | Generation of 3D point cloud | 5 | N/A | N/A | < 3 | < 3 |
| 2015 | LIDAR | Direct measurements | 2.5 | N/A | N/A | <1 | <1 |
| 2017 | ASI | Generation of 3D point cloud | 2.5 | N/A | N/A | <2 | <2 |
| 2019 | ASI | Generation of 3D point cloud | 2.5 | N/A | N/A | <2 | <2 |
| 2021 | ASI | Generation of 3D point cloud | 2.5 | N/A | N/A | <2 | <2 |

Table S4. Data processing strategy for the reconstruction of the ice-covered bedrock. GPR – ground probing radar; ERT – electrical resistivity tomography.

| Year | Data source | Process | Transducer (MHz) | Wavelength - λ in ice (m) | Vertical resolution $\lambda/8$ criterion / cell size (m) |
|------|-------------|---------------------|------------------|-----------------------------------|---|
| 2004 | GPR | Geophysical imaging | 35 | 4.71 | 0.60 |
| 2004 | GPR | Geophysical imaging | 100 | 1.65 | 0.20 |
| 2015 | GPR | Geophysical imaging | 500 | 0.33 | 0.04 |
| 2017 | GPR | Geophysical imaging | 200 | 0.83 | 0.10 |
| 2018 | GPR | Geophysical imaging | 500 | 0.33 | 0.04 |
| 2022 | GPR | Geophysical imaging | 500 | 0.33 | 0.04 |
| 2017 | ERT | Geophysical imaging | N/A | N/A | 1.00 |

Table S5. Synopsis of the data sources used in the study.**a. Aerial and satellite images**

| Year | Type of survey | Scale | Institution/Company |
|------|----------------|----------|---------------------------|
| 1945 | Aerial | 1:33,000 | IGM |
| 1954 | Aerial | 1:33,000 | GAI (contracted by IGM) |
| 1973 | Aerial | 1:33,000 | EIRA (contracted by PAT) |
| 1982 | Aerial | 1:33,000 | REVEN |
| 1988 | Aerial | 1:33,000 | CGR (contracted by PAT) |
| 1991 | Aerial | 1:33,000 | REVEN |
| 1992 | Aerial | 1:33,000 | REVEN |
| 1994 | Aerial | 1:33,000 | CGR (contracted by PAT) |
| 2000 | Aerial | 1:33,000 | TerraItaly, PAT |
| 2001 | Aerial | 1:33,000 | REVEN |
| 2003 | Aerial | 1:33,000 | PAT |
| 2006 | Aerial | 1:33,000 | CGR (contracted by PAT) |
| 2008 | Aerial | 1:33,000 | AGEA |
| 2009 | Aerial | 1:33,000 | PAT |
| 2011 | Aerial | 1:33,000 | AGEA |
| 2012 | Aerial | 1:33,000 | REVEN |
| 2014 | Aerial | 1:33,000 | CTA |
| 2015 | Satellite | | BING |
| 2015 | Aerial | 1:33,000 | TERRA (contracted by PAT) |
| 2017 | Satellite | | AGEA |
| 2019 | Aerial | 1:33,000 | SAT |
| 2021 | Satellite | | AGEA |
| 2021 | Satellite | | ESRI WORLD IMAGERY |
| 2022 | Satellite | | PLEIADES NEO |

b. Historical Cartography and cartography

| Year | Title of the map | Scale | Institution/Company |
|------|-------------------------------|-----------|---------------------------|
| 1874 | Karte der Dolomit Alpen | 1:100,000 | P. Ritter von Wiedenmann |
| 1885 | Karte der Alpen Tyrol | 1:600,000 | Jos. Ant. Finsterlin |
| 1888 | Monte Marmolada, F11, II, NE | 1:25,000 | IGM |
| 1903 | Übersichtskarte der Dolomiten | 1:100,000 | G. Freytag & Berndt, Wien |
| 1903 | Monte Marmolada, F11, II, NE | 1:25,000 | IGM |
| 1905 | Karte der Marmolata Gruppe | 1:25,000 | G. Freytag & Berndt, Wien |
| 1926 | Karte der Marmolata Gruppe | 1:25,000 | G. Freytag & Berndt, Wien |
| 1932 | Monte Marmolada, F11, II, NE | 1:25,000 | IGM |
| 1963 | Monte Marmolada, F11, II, NE | 1:25,000 | IGM |
| 1971 | Ghiacciaio della Marmolada | 1:25,000 | Rossi, CGI |

c. Recent maps

| Year | Title of the map | Scale | Institution/Company |
|------|------------------------------------|----------|---------------------|
| 1981 | Carta Tecnica Regionale del Veneto | 1:10,000 | REVEN |
| 1982 | Carta Tecnica Regionale del Veneto | 1:10,000 | REVEN |
| 1986 | Monte Marmolada, F11, II, NE | 1:25,000 | IGM |
| 2015 | Carta Tecnica Provinciale | 1:10,000 | PAT |
| 2016 | Carta Tecnica Regionale del VENETO | 1:10,000 | REVEN |
| 2021 | Carta Tecnica Provinciale | 1:10,000 | PAT |

d. LIDAR & TLS surveys

| Year | Grid size (m) | Type | Institution/Company |
|------|---------------|-----------|---------------------|
| 2009 | 1x1 | LIDAR | PAT |
| 2011 | 1x1 | LIDAR | PAT |
| 2014 | 1x1 | LIDAR | PAT |
| 2014 | 1x1 | LIDAR | ARPAV |
| 2022 | 0.1x0.1 | TLS | OGS, UNIPR |
| 2022 | 0.05x0.05 | UAV LIDAR | OGS, UNIPR |

e. GPR surveys

| Year | Type / antenna frequency (MHz) | Overall scan (km) | Institution/Company |
|------|---|-------------------|-----------------------------|
| 2004 | single Channel / 70 single Channel / 100 | 18.5 | UNIGE (contracted by ARPAV) |
| 2015 | single channel / 500 | 0.5 | UNIPD, UNIPR & OGS |
| 2017 | multichannel / 200 | 54.0 | UNIPD, UNIPR & OGS |
| 2018 | single channel / 500 | 3.5 | UNIPR & OGS |
| 2022 | single channel / 50 | 1.0 | UNIPR & OGS |
| | single channel / 200 | 0.3 | |

Glossary

| Acronym | Name (Italian) | Description (English) |
|---------|---|--|
| AGEA | Agenzia per le Erogazioni in Agricoltura | <i>Funding Agency for Agriculture</i> |
| ARPAV | Agenzia Regionale per la Prevenzione e Protezione Ambientale del Veneto | <i>Environmental Prevention and Protection Agency of the Veneto Region</i> |
| BING | Microsoft Bing | <i>Microsoft Bing</i> |
| CAI | Club Alpino Italiano | <i>Italian Alpine Club</i> |
| CGR | Compagnia Generale Riprese Aeree | <i>General Contractor for Aerial Surveys</i> |
| CGI | Comitato Glaciologico Italiano | <i>Italian Glacial Committee</i> |
| CTA | Consorzio Telerilevamento Agricoltura | <i>Remote Sensing Consortium for Agriculture</i> |
| CTP | Carta Tecnica Provinciale (1:5,000; 1:10,000) | <i>Digital Vector Map of the Province of Trento</i> |
| CTRVN | Carta Tecnica Regionale Numerica del Veneto (1:5,000; 1:10,000) | <i>Digital Vector Map of the Veneto Region</i> |
| EIRA | Ente Italiano Rilievi Aerofotogrammetrici | <i>Italian Institute for Aerophotogrammetric Surveys</i> |
| ENEL | Ente Nazionale Energia Elettrica | <i>National Electric Company</i> |
| ESRI | | <i>Environmental Systems Research Institute</i> |
| GAI | Gruppo Aereo Italiano | <i>Italian Air Group</i> |
| IGM | Istituto Geografico Militare Italiano | <i>Italian Military Geographical Institute</i> |
| OGS | Istituto Nazionale di Oceanografia e di Geofisica Sperimentale | <i>National Institute of Oceanography and Applied Geophysics</i> |
| PAT | Provincia Autonoma di Trento | <i>Autonomous Province of Trento</i> |
| REVEN | Regione del Veneto | <i>Veneto Region</i> |
| SAT | Società Alpinisti Tridentini | <i>Tridentine Society of Alpinists</i> |
| TERRA | Terra Messflug GmbH | <i>Terra Messflug GmbH</i> |
| UNIPD | Università degli Studi di Padova | <i>University of Padova</i> |
| UNIPR | Università degli Studi di Parma | <i>University of Parma</i> |

Acknowledgements

The Authors thank Provincia Autonoma di Trento and Regione del Veneto for making cartography data and aerial/satellite images available. The authors are also grateful to Land Technology & Services Srl for extracting the point clouds from the overlapping aerial and satellite images and for processing IR images.

References

- Acock, M.C., Pachepsky Ya.A.: Estimating Missing Weather Data for Agricultural Simulations Using Group Method of Data Handling, *J. Appl. Meteor.* 39, 7, 1176–1184, doi:10.1175/1520-0450, 2000.
- Aggarwal, A., Jain, S.K., Lohani, A.K., and Jain, N.: Glacial lake outburst flood risk assessment using combined approaches of remote sensing, GIS and dam break modelling, *Geomatics Natural Hazards and Risk*, 7, 1, 18–36, 2016.
- Antonelli, R., Barbieri, G., Dal Piaz, G. V., Dal Pra, A., De Zanche, V., Grandesso, P., Mietto, P., Sedeà, R., and Zanferrari, A.: Carta geologica del Veneto 1: 250.000 - Una Storia di cinquecento milioni di anni, *Geological Map of the Veneto Region 1:250,000*, 32 pp, 1990.
- Bosellini, A.: *Geologia delle Dolomiti*, Athesia. ISBN-13: 9788870148893, 1996.
- Bocchia, F., Francese, R., Giorgi, M., Fischanger, F., and Picotti, S.: The impact of multiple transmitters on signal strength in Deep Electrical Resistivity Tomography data: an experiment in the Vajont valley (north-eastern Italy), *Bulletin of Geophysics and Oceanography*, 62, 4, 687-706, doi:10.4430/bgta0359, 2021.
- Böeckli, L., Brenning, A., Gruber, S., and Nötzli, J.: Permafrost distribution in the European Alps: calculation and evaluation of an index map and summary statistics, *The Cryosphere*, 6, 807-820, doi:10.5194/tc-6-807-2012, 2012.
- Bondesan, A., and Francese, R.: The climate-driven disaster of the Marmolada Glacier (Italy), *Geomorphology*, SI, 431, doi:10.1016/j.geomorph.2023.108687, 2023.
- Carton, A., and Varotto, M.: *Marmolada*, CierreEdizioni, Dipartimento di Geografia Univ. Padova, 413 pp, 2011.
- Carton, A., Bondesan, A., and Benetton, S.: *Marmolada, la regina della Dolomiti*, Itinerari Glaciologici sulle Montagne Italiane 3, Itinerari 19A e 19B, 89–212, 2017.
- ENEA, Ente per le Nuove tecnologie, l'Energia e l'Ambiente: Atlas of the solar radiation. <http://www.solaritaly.enea.it/CalcRggmmIncl/Calcola3.php>, 2023.
- Etzelmüller, B., Guglielmin, M., Hauck, C., Hilbich, C., Hoelzle, M., Isaksen, K., Noetzli, J., Oliva, M. and Ramos, M.: Twenty years of European mountain permafrost dynamics – the PACE legacy, *Environmental Research Letters*, 15, 104070, doi:10.1088/1748-9326/abae9d, 2020.
- Huggel, C., Kääb, A., Haeblerli, W., Teyssie, P., and Paul, F.: Remote sensing based assessment of hazards from glacier lake outbursts: A case study in the Swiss Alps, *Canadian Geotechnical Journal*, 39, 2, 316 – 330, 2002.
- Janbu, N.: Application of composite slip surface for stability analysis. *Proceedings of European conference on stability of earth slopes*, Stockholm, 3, 43 – 49, 1954.
- Janbu, N., Bjerrum, L. and Kjaernsli, B.: *Soil mechanics applied to some engineering problems*. Norwegian Geotechnical Institute Publication 16, Oslo, Norway, 1956.
- Janbu, N.: Slope stability computations, in: *Embankment Dam Engineering*, Casagrande Memorial Volume (eds E. Hirsch-field and S. Poulos), 47 – 86, New York: Wiley, 1973.

Kotsiantis, S., Kostoulas, A., Lykoudis, S., Argiriou, A., Menagias, K.: Filling missing values in weather data banks, 2nd IEE International Conference on Intelligent Environments, 5-6 July, 2006, Athens, Greece 1, 327-334, doi:10.1049/cp:2006065925, 2006.

Krige D.G.: Two-dimensional weighted moving average trend surfaces for ore-valuation, in Proc. Symposium on Mathematical Statistics and Computer Applications in Ore Valuation: J. South Afr. Inst. Min. Metall., Johannesburg, 1966, Mar. 7-8, 13-38, 1996.

LaBrecque, D.J., Morelli, G., Fischanger, F., Lamoureux, P., and Brigham, R.: Field trials of the multi-source approach for resistivity and induced polarization data acquisition, in: Proceedings of the 2013 AGU Fall Meeting, American Geophysical Union, abstract NS34A-03, December 9–13, San Francisco, USA, 2013.

Ledig, C., Theis, L., Huszár, F., Caballero, J., Cunningham, A., Acosta, A., Aitken, A., Tejani, A., Totz, J., Wang, Z., and Shi, W.: Photo-realistic single image super-resolution using a generative adversarial network, Proc. 30th IEEE Conference on Computer Vision and Pattern Recognition, CVPR, 2017.

Lee W.H., and Lahr, J.C.: Hypo71 (revised): a computer program for determining local earthquake hypocentral parameters, magnitude, and first motion pattern of local earthquakes. US Geol. Survey Open-file Report 75-311, doi:10.3133/ofr75311, 1975.

Liebel, L., and Körner, M.: Single-image super resolution for multispectral remote sensing data using convolutional neural networks, International Archives of the Photogrammetry, Remote Sensing and Spatial Information Sciences - ISPRS Archives, 41, 883–890, 2016.

Lomax, A., Satriano, C., and Vassallo, M.: Automatic picker developments and optimization: FilterPicker--a robust, broadband picker for real-time seismic monitoring and earthquake early warning, Seismological Research Letters, 83, 3, 531–540, doi:10.1785/gssrl.83.3.531, 2012.

MATLAB: 9.7.0.1190202 (R2019b), Natick, Massachusetts: The MathWorks Inc, 2018.

McFeeters, S.K.: The use of the Normalized Difference Water Index (NDWI) in the delineation of open water features, International Journal of Remote Sensing, 17, 7, 1425–1432, 1996.

Madhukar, B.N., and Narendra, R.: Lanczos Resampling for the Digital Processing of Remotely Sensed Images, Proceedings of VCASAN-2013, Lecture Notes in Electrical Engineering; Springer; 258, 403–411, 2013.

Morgenstern, N.R., and Price, V.E.: The analysis of the stability of general slip surfaces, Geotechnique, 15, 1, 79–93, 1965.

Pasta, M.: Esecuzione ed interpretazione di misure georadar sul ghiacciaio della Marmolada e studi di fattibilità su ghiacciai del Fradusta e dell'Antelao Superiore, ARPAV, Technical Report, 20 pp, 2004.

Pellicciotti, F., Brock, B., Strasser, U., Burlando, P., Funk, M., and Corripio, J.: An enhanced temperature-index glacier melt model including the shortwave radiation balance: Development and testing for Haut Glacier d'Arolla, Switzerland, J. Glaciol., 51, 175, 573–587, doi:10.3189/172756505781829124, 2005.

Siebert S., Teizer, J.: Mobile 3D Mapping for Surveying Earthwork Projects using an Unmanned Aerial Vehicle (UAV) System, Autom. Constr., Elsevier, 41, 1–14, doi:10.1016/j.autcon.2014.01.004, 2014.

Varotto, M., and Ferrarese, F.: Esperienze di contrasto e mitigazione dei cambiamenti climatici: il ghiacciaio della Marmolada, *Tecnologie e progetti*, 20-31, 2021.

Wang X., Yang T., Xu C., Xiong L., Shi P., Li, Z.: The response of runoff components and glacier mass balance to climate change for a glaciated high-mountainous catchment in the Tianshan Mountains, *Natural Hazards*, 104, 1239–1258, doi:10.1007/s11069-020-04212-4, 2020.

Widess, M.B.: How thin is a thin bed? *Geophysics*, 38, 6, 1176–1180, doi:10.1190/1.1440403, 1973.

Yue X., Li Z., Zhao, J., Fan, J., Takeuchi, N., Wang. L.: Variation in albedo and its relationship with surface dust at Urumqi Glacier No. 1 in Tien Shan, China, *Front. Earth Sci.*, 8, 110, doi:10.3389/feart.2020.00110, 2020.